Supplementary Information

Capturing Exciton–Proton Collisions in Confined Water

Ziyi Wang,[1] Jacek Kłos,[2,3] Jacob Fortner,[4] YuHuang Wang[1,4,5]*

[1]Department of Chemistry and Biochemistry, University of Maryland, College Park, Maryland 20742, United States
[2]Department of Physics, University of Maryland, College Park, Maryland 20742, United States
[3]Joint Quantum Institute, University of Maryland, College Park, Maryland 20742, United States
[4]Chemical Physics Program, University of Maryland, College Park, Maryland 20742, United States
[5]Maryland NanoCenter, University of Maryland, College Park, Maryland 20742, United States
*Corresponding author. Email address: yhw@umd.edu

List of Supplementary Materials

Supplementary Video S1. Computational visualization of an exciton–proton collision. Quantum chemical model illustrating how the defect-localized excitonic wavefunction evolves as an ion (red dot) approaches along a (6,5)-SWCNT nanopore. This visualization highlights the strong local-field sensitivity of defect-trapped excitons to protons confined within single-file water chains, providing a conceptual framework for interpreting the discrete spectral and intensity changes observed experimentally.

Supplementary Video S2. Repeated exciton–proton collisions at the same defect site in a short (6,5)-SWCNT pore under pH 2 conditions. Time trace of E_{sp3} photoluminescence from a single defect site in a TIP device exposed to an acidic aqueous solution (pH 2.0). The data are recorded from the same atomic defect site throughout the experiment. Discrete intensity steps (highlighted in red) arising from reversible spectral shifts correspond to individual proton trapping and de-trapping events at the same defect site. The black trace provides a background reference. This TIP device is identical to that shown in Supplementary Fig. 17 and Fig. 4 of the main text.

Supplementary Video S3. Suppressed exciton–proton collision frequency at a defect site deep within a long nanotube pore. Time trace of defect-trapped exciton PL from a defect site located deep within a long (6,5)-SWCNT TIP device exposed to a pH 2.0 aqueous solution. Compared to short nanotubes, discrete proton trapping events (red markers) occur with significantly reduced frequency, consistent with limited proton access to defect sites located far from the pore opening. The black trace indicates background intensity. This TIP device corresponds to Supplementary Fig. 19 and serves as a spatial-accessibility control.

Supplementary Figs. 1–21.

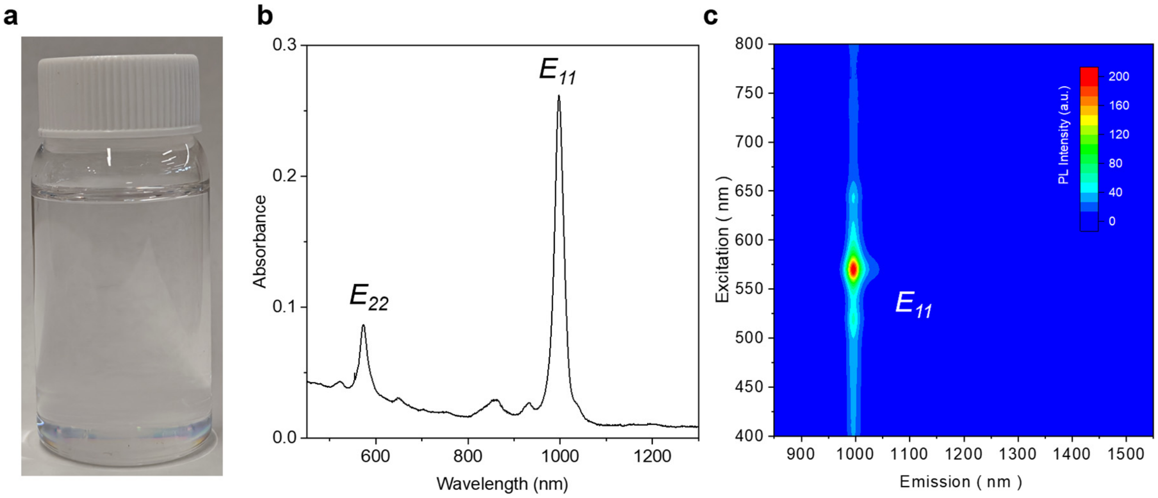

Supplementary Fig. 1. Optical characterization of purified (6,5)-SWCNTs prior to defect incorporation. **a**, Photograph of a solution of chirality-purified (6,5)-SWCNTs stabilized by PFO-bPy in toluene. **b**, Absorption spectrum showing the dominant E_{11} excitonic transition at ~980 nm and the corresponding E_{22} transition at higher energy. **c**, Excitation-emission (PLE) map confirming nearly single-chirality purity and the absence of native defects.

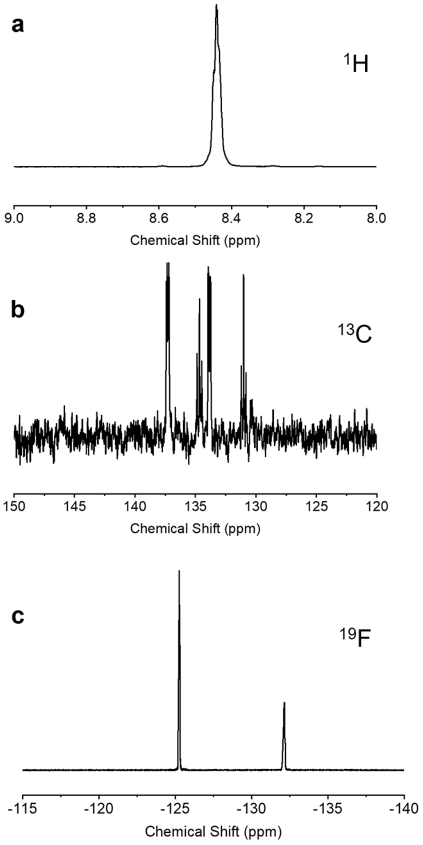

Supplementary Fig. 2. Chemical characterization of the diazonium precursor used to create sp^3 quantum defect traps. a, ^{1}H, **b**, ^{13}C, and **c**, ^{19}F-NMR spectra of synthesized 3,4,5-trifluorobenzene diazonium tetrafluoroborate in acetonitrile-d_3. The spectra confirm the expected molecular structure and chemical purity of the diazonium salt used to generate sp^3 quantum defects on (6,5)-SWCNTs. This controlled defect precursor enables the reproducible formation of well-defined, isolated exciton traps, which serve as the interaction sites for exciton–proton collisions investigated in this work.

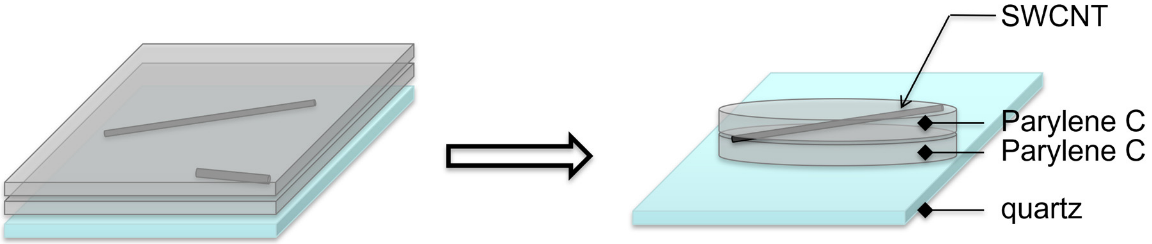

Supplementary Fig. 3. Trap-in-a-pore (TIP) architecture for isolating single exciton–proton interactions. Schematic illustration of individual single-walled carbon nanotubes (SWCNTs) encapsulated between two Parylene C layers deposited on a quartz substrate. Lithographically patterned Parylene C protection pads selectively expose only the nanotube ends, forming an accessible nanotube pore while electrically and chemically isolating the remainder of the nanotube. This geometry confines small aqueous species to the nanotube interior while spatially isolating defect-localized excitons from the external environment, enabling repeated measurements of exciton–proton collisions at the same atomic defect site within a single nanotube pore.

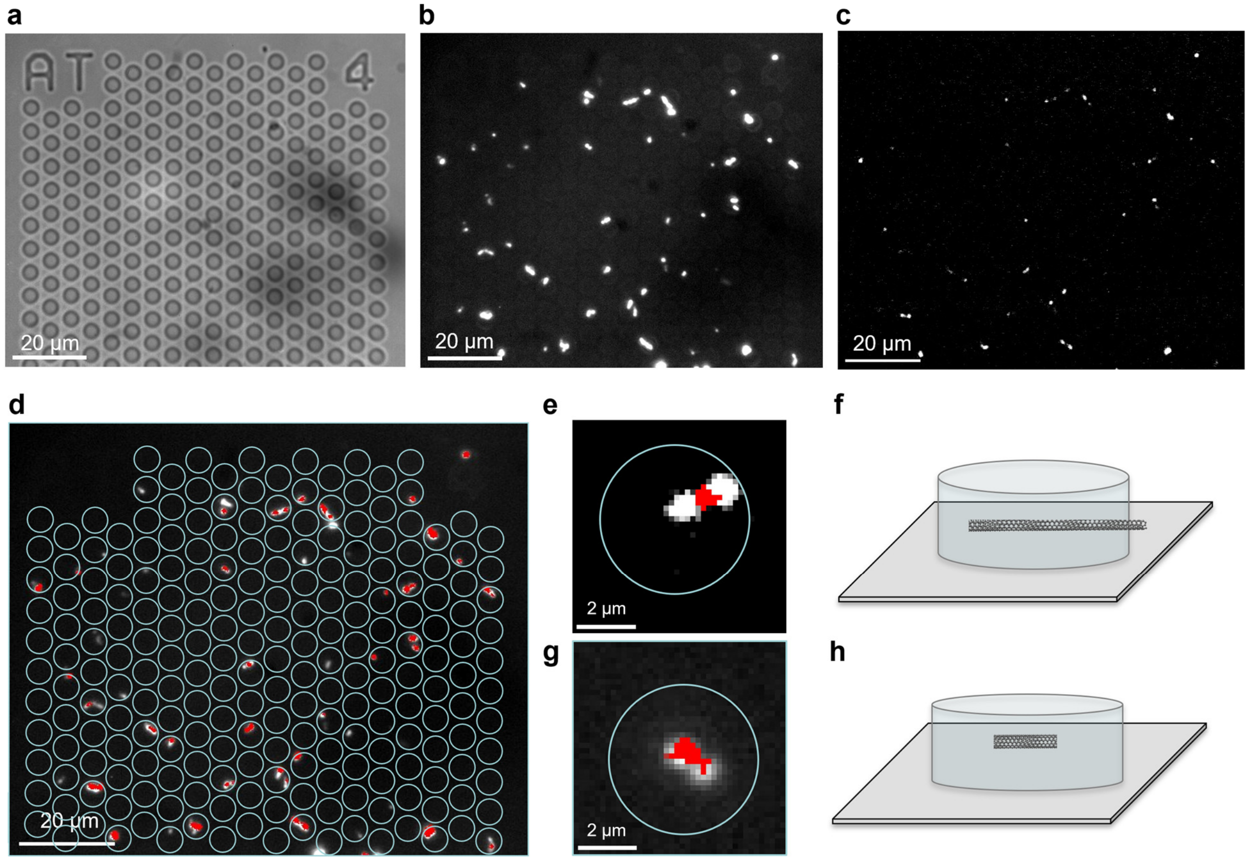

Supplementary Fig. 4. Optical identification of individual nanotubes, defect-localized exciton PL, and pore accessibility in a TIP array. a, White-light optical image of a lithographically patterned TIP array showing the 5 µm-diameter Parylene C protection pads. The alphanumeric labels indicate array locations on the chip. **b**, Corresponding PL image of individual (6,5)-SWCNTs under 561 nm laser excitation, showing spatially isolated nanotubes within individual pads. **c**, Defect-localized exciton PL (E_{sp3}) from the same field of view, which is spectrally redshifted relative to mobile E_{11} exciton emission and arises from individual sp^3 quantum defect sites. **d**, Composite image overlaying the nanotube exciton PL (white), defect-localized exciton PL (red), and Parylene C pad boundaries (cyan), enabling unambiguous assignment of defect emission to individual nanotubes within a defined pore geometry. (**e–f**) PL imaging and schematic illustrations of representative partially encapsulated nanotubes with exposed ends (TIP configuration, enabling access of water and protons to the nanotube interior) and fully encapsulated nanotubes (sealed controls), respectively. These configurations distinguish proton-accessible pores from encapsulated nanotubes that serve as negative controls throughout this work.

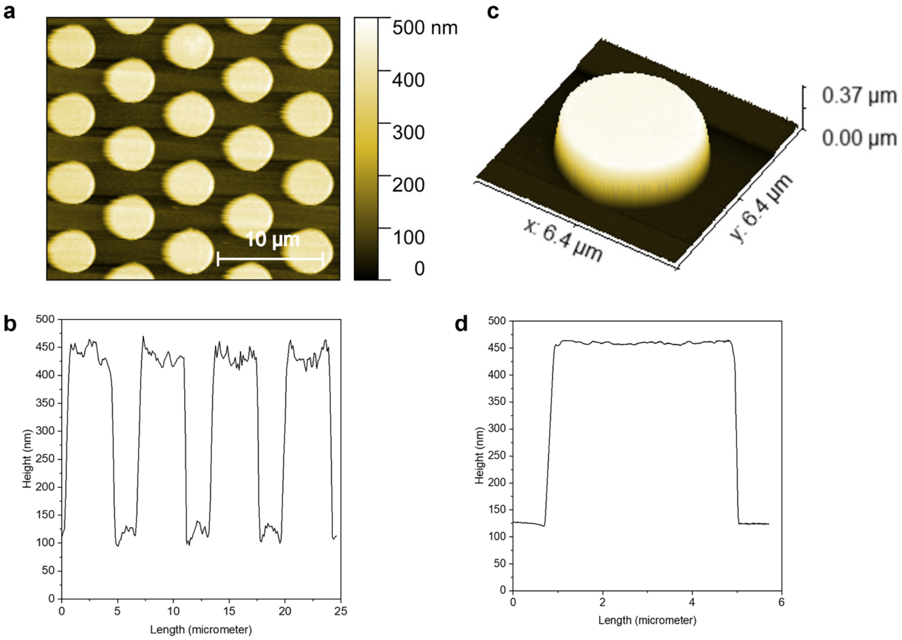

Supplementary Fig. 5. AFM characterization of lithographically patterned Parylene C pads that enable controlled nanotube pore access. **a**, Topographic AFM image of a representative array of Parylene C protection pads patterned on quartz, showing uniform circular pads with diameters of approximately 4.5 μm. **b**, AFM height profile showing 325 nm thickness, corresponding to two stacked Parylene C layers used to encapsulate and protect the nanotube body. **c**, Three-dimensional AFM rendering and **d**, high-resolution height profile of a representative pad showing the well-defined pad boundaries that spatially confine the exposed nanotube pore region.

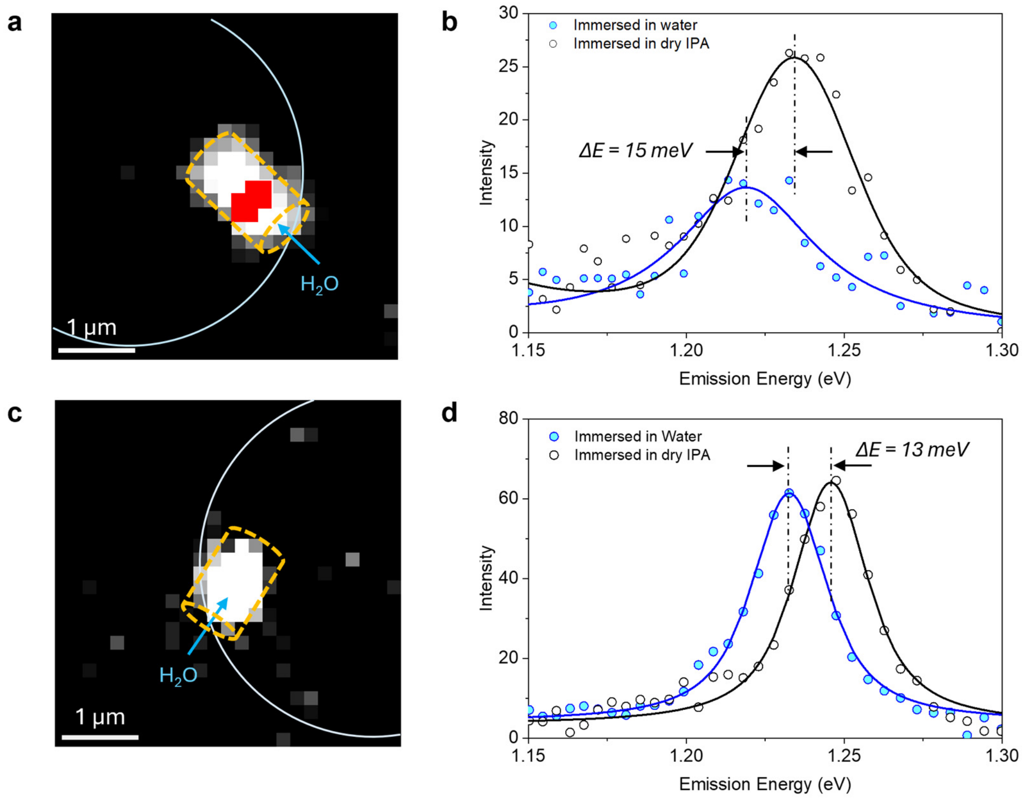

Supplementary Fig. 6. Water filling of individual TIP devices probed by nanotube photoluminescence. PL spectra of two individual (6,5)-SWCNTs: **a**, a representative TIP device, and **b**, a pristine (6,5)-SWCNT control. In each case, measurements were performed on the same individual nanotube or TIP device under dry isopropanol (empty pore) and water (filled pore). Water filling induces a reproducible redshift of the nanotube E_{11} exciton PL peak by 15 meV and 13 meV for these two representative nanotubes, respectively, relative to their empty state.

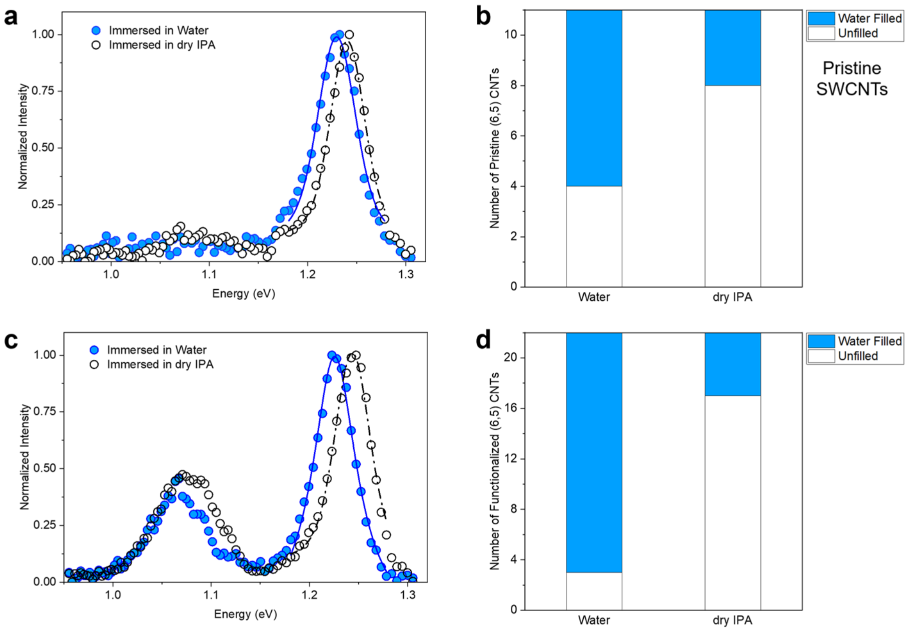

Supplementary Fig. 7. Statistical characterization of water accessibility and excitonic responses across multiple TIP devices. a, Averaged PL spectra of 11 individual, defect-free (6,5)-SWCNTs measured under water-filled (blue solid circles) and empty (dry IPA, black open circles) conditions. Each spectrum represents an average over independently identified single nanotubes. **b**, Histogram showing the fraction of defect-free nanotubes that exhibit water-induced E_{11} redshifts, indicating pore accessibility following lithographic processing. **c**, Averaged PL spectra of 22 individual TIP devices, showing distinct spectral responses to water and dry IPA. **d**, Histogram of water-filled versus unfilled TIP devices, demonstrating that defect incorporation does not suppress pore accessibility. All measurements were performed on individual nanotubes under 561 nm laser excitation at 54.3 W/cm^2.

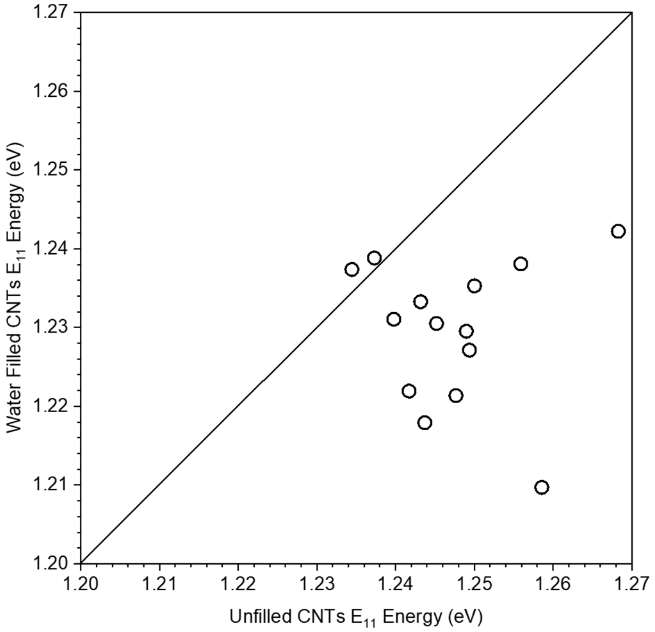

Supplementary Fig. 8. Statistical analysis of the spectral shifts in (6,5)-SWCNT exciton PL (E_{11}) upon reversible water filling of individual TIP nanotube pores. E_{11} PL peak positions of 14 individual TIP devices were extracted by fitting with a Voigt function and compared between water-filled and empty states. Twelve out of the 14 TIP nanotubes exhibited a reproducible redshift in the E_{11} exciton PL peak upon water filling, confirming pore accessibility following lithographic processing. These measurements establish a quantitative, nanotube-by-nanotube criterion for identifying water-accessible pores prior to defect-localized exciton and proton-interaction studies.

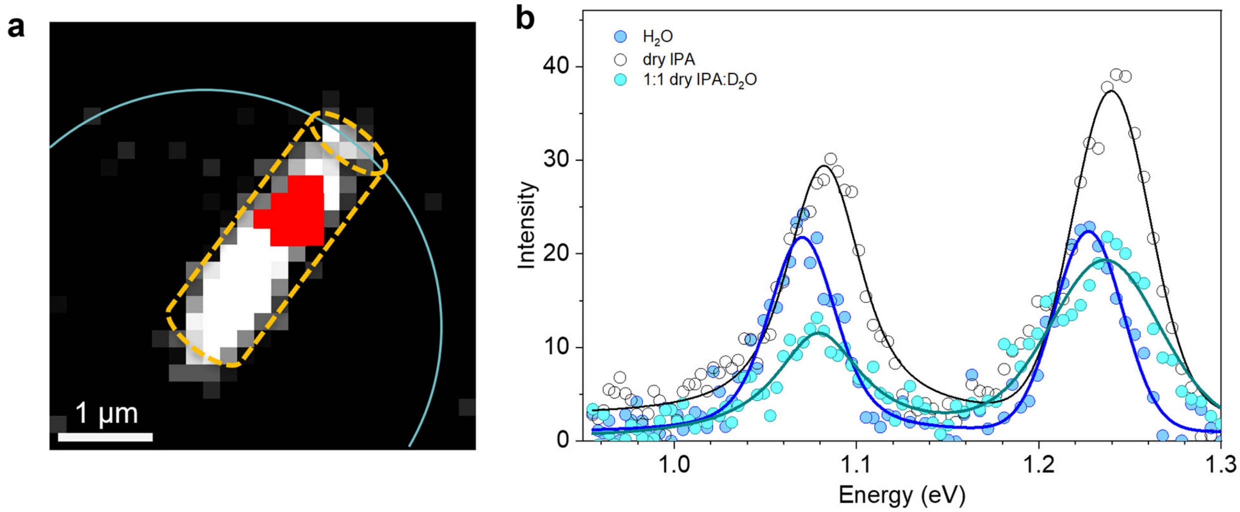

Supplementary Fig. 9. Isotope-dependent spectral responses of defect-trapped excitons to H_2O and D_2O filling in a TIP nanotube pore. (**a**) PL image of a TIP device containing an individual (6,5)-SWCNT with a single sp3 quantum defect trap. Emission from defect-trapped E_{sp3} excitons (red) is superimposed on the E_{11} exciton PL. (**b**) PL peak position of the same nanotube and the same defect site monitored under sequential filling with H_2O (pH 6.0), dry IPA (empty), and a 1:1 IPA-D_2O mixture. The nanotube exciton (E_{11}) and defect-trapped exciton (E_{sp3}) PL show distinct spectral responses to H_2O and D_2O filling.

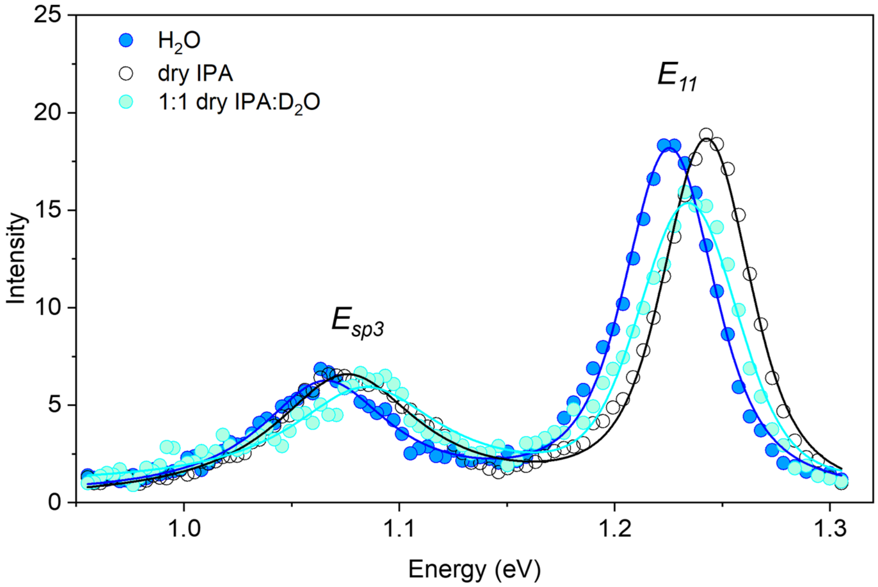

Supplementary Fig. 10. PL responses of nanotube E_{11} excitons and defect-localized E_{sp3} excitons to H_2O and D_2O averaged over 26 individual (6,5)-SWCNTs. For each TIP nanotube, measurements were performed sequentially under H_2O-filled, dry IPA (empty pore), and 1:1 vol.: vol. IPA-D_2O conditions to ensure comparisons on the same nanotube. Water filling induces a redshift in E_{11} emission from 1.243 ± 6 meV (dry IPA) to 1.225 ± 5 meV, which is reversed upon dehydration with IPA. Refilling with D_2O produces similar but smaller redshifts. In contrast, defect-localized excitons exhibit a qualitatively different isotope response: D_2O filling results in a blueshift from 1.073 ± 15 meV (dry IPA) to 1.084 ± 23 meV, whereas H_2O filling induces a redshift to 1.064 ± 19 meV. This opposing isotope dependence of defect-localized excitons is observed consistently across individual TIP nanotubes, supporting a mechanism involving proton-specific interactions and hydration dynamics at sp^3 quantum defect sites, rather than generic dielectric effects.

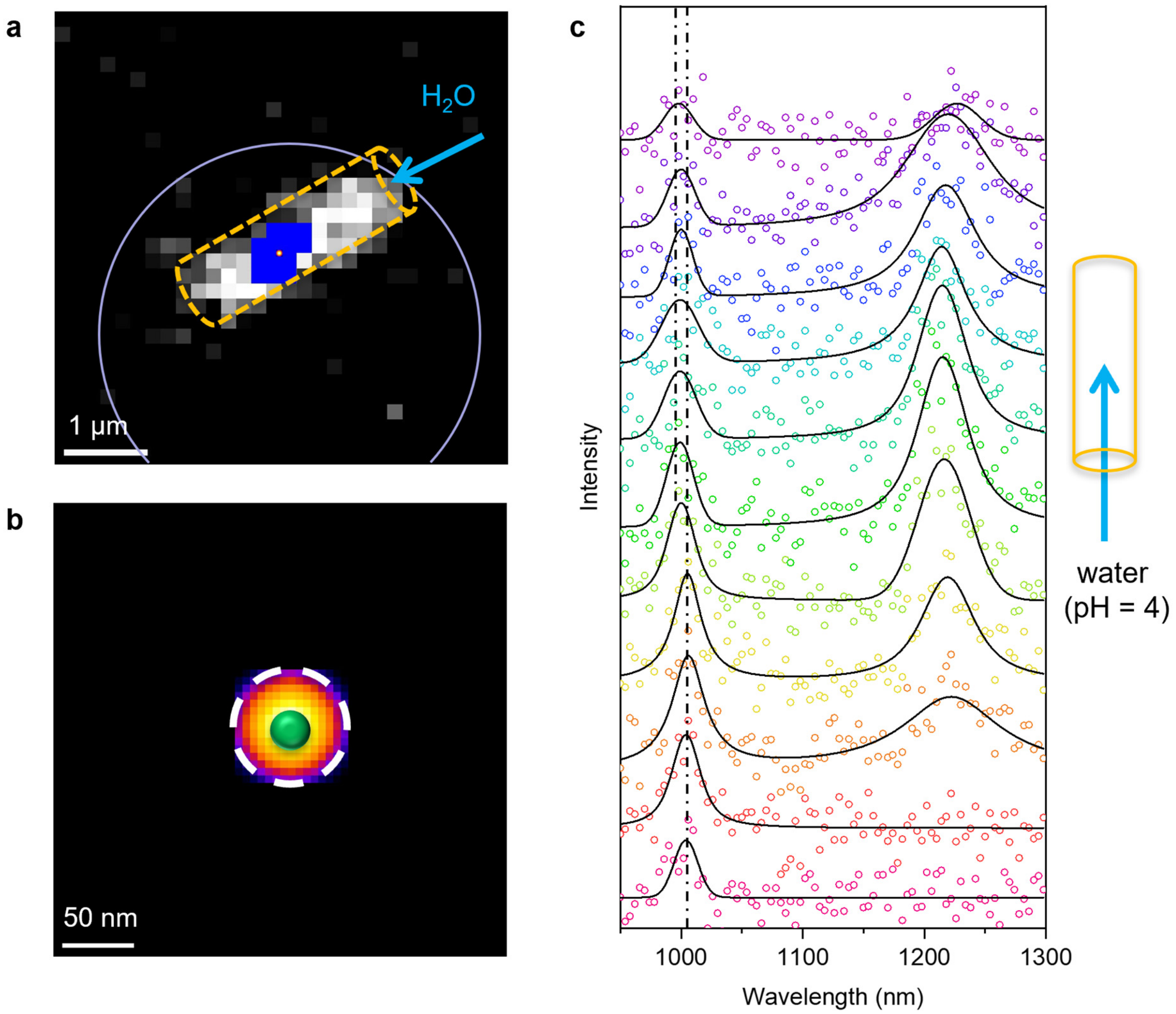

Supplementary Fig. 11. Extended data set of Fig. 2D on the spectral responses of nanotube and defect-trapped excitons to water filling. a, PL image of a TIP (6,5)-SWCNT bearing a single sp^3 quantum defect (3,4,5-trifluorobenzene/OH). Emission from the defect-localized exciton (E_{sp3}) is spectrally separated from the nanotube E_{11} emission. **b,** Super-resolution localization of the same defect exciton trap. **c,** Hyperspectral line scans acquired along the nanotube axis under exposure to a pH=4.0 aqueous solution. Photoluminescence spectra were recorded under 561 nm laser excitation at 54.3 W/cm^2.

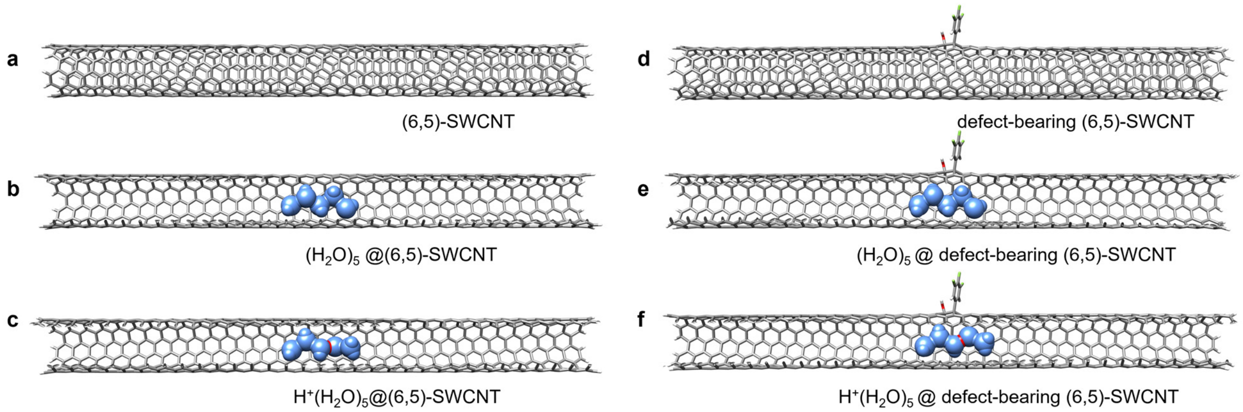

Supplementary Fig. 12. Atomistic models of water-filled and proton-containing water chains in pristine and defect-bearing nanotube pores. DFT-optimized atomistic models used to simulate the spectral response of excitons to protons in confined water: (**a–c**) Representative atomic configurations of a pristine (6,5)-SWCNT containing (a) an empty nanotube pore, (b) a single-file water chain ($(H_2O)_5$), and (c) a proton-containing water chain ($H^+@(H_2O)_5$). **(d–f)** Corresponding configurations in a (6,5)-SWCNT bearing a single sp3 quantum defect (3,4,5-trifluorobenzene/OH), including (d) an empty pore, (e) a neutral water chain, and (f) a proton-containing water chain. The red sphere represents H^+, while the light blue spheres denote neutral H_2O molecules. All geometries were optimized at the CAM-B3LYP/3-21G level of theory.

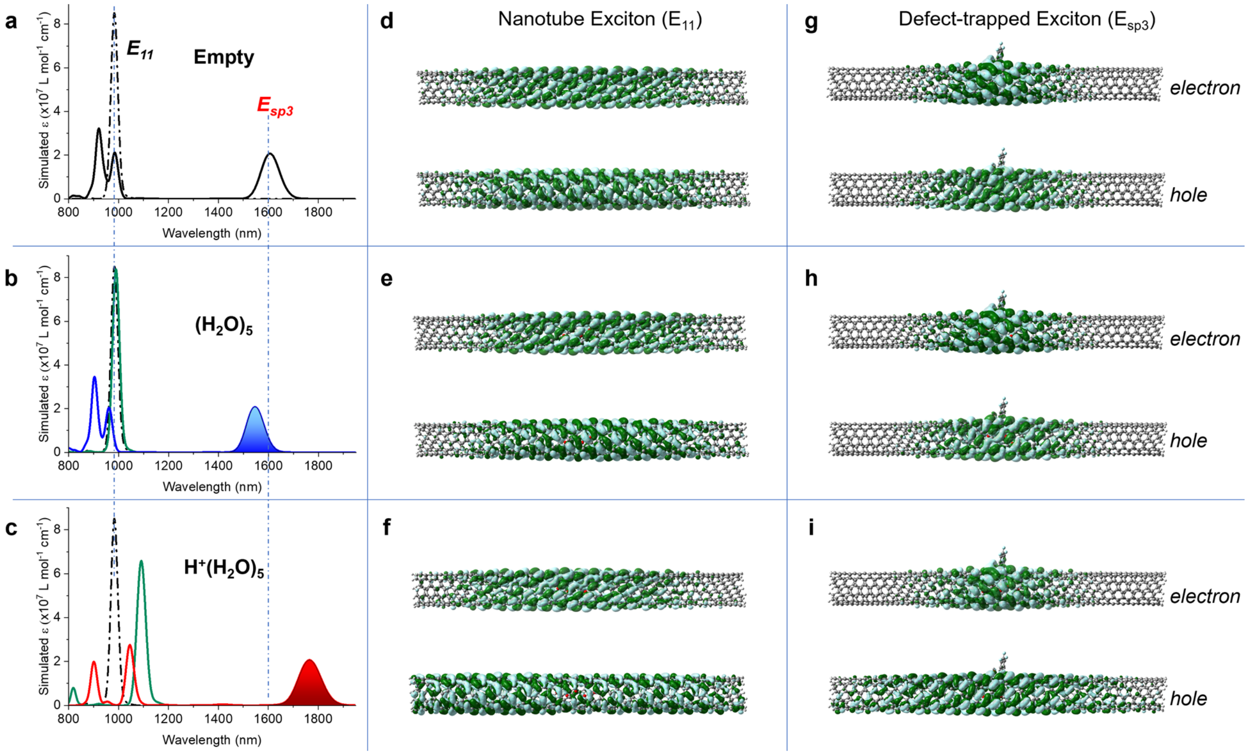

Supplementary Fig. 13. Proton-induced modification of defect-localized excitonic states in nanotube pores. Simulated electronic absorption spectra and corresponding natural transition orbitals (NTOs). (**a–c**) Computed electronic absorption spectra highlighting distinct spectral shifts in E_{11} and E_{sp3} upon introducing $(H_2O)_5$ (b) or $H^+(H_2O)_5$ (c) into empty (a) SWCNTs. Calculations were performed on an 8-nm-long, defect-free nanotube (green curves) and on a nanotube bearing a quantum defect (3,4,5-trifluoro benzene/OH), with the defect exciton peak indicated by shading. The spectra were calculated using TD-DFT (CAM-B3LYP/3-21G) and corrected by applying a -0.580 eV shift to align the E_{11} transition of the pristine empty model with the experiment. A Gaussian linewidth of 25 meV at 298.15 K was used.

(**d–i**) Natural transition orbitals (NTOs) illustrating the electron and hole wavefunctions of (d-f) the nanotube E_{11} exciton in response to (e) $(H_2O)_5$ and (f) $H^+(H_2O)_5$, and (g-i) the defect-trapped E_{sp3} exciton under the same conditions. All calculations were carried out using TD-DFT at the CAM-B3LYP/3-21G level.

Theoretical Model of Exciton-Ion Collisions. To simulate exciton-proton interactions inside a nanotube pore, we modeled a (6,5)-SWCNT as a hollow cylindrical shell of finite length *L* and radius *R*, capturing the essential electrostatic coupling between a defect-localized exciton and a proton inside the nanotube (Supplementary Fig. 14). This minimal model interprets exciton–proton collision dynamics observed experimentally.

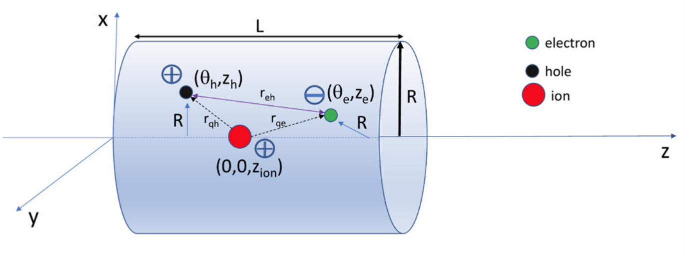

Supplementary Fig. 14. Cylindrical shell model for exciton–proton interactions in a nanotube. The nanotube is represented as a hollow cylindrical shell of radius R and length L, with the axial (z) and angular (θ) coordinates defining the relative positions of the electron and hole comprising the exciton. The electron (green) and hole (black) are confined to the nanotube surface at coordinates (θ_e, z_e) and (θ_h, z_h), respectively, while the ion (red), representing a hydrated proton, is treated as a point charge located along the nanotube axis at position $(0, 0, Z_{ion})$. Distances between the ion and charge carriers (r_{qe}, r_{qh}) and the electron–hole separation (r_{eh}) define the Coulomb interactions included in the variational exciton Hamiltonian.

The nanotube is represented as a cylindrical shell with radius $R = 7.05\, a_0$ and length $L = 300\, a_0$, corresponding to a diameter of approximately 0.7 nm and a length of 15 nm. The electron and hole forming the exciton are described in cylindrical coordinates (z_e, θ_e) and (z_h, θ_h), respectively. The ion, carrying a point charge, is treated as a point charge located along the nanotube axis at position $(0, 0, z_q)$.

The exciton is described using a variational trial wavefunction,
$\psi_{\text{trial}}(n_h, m_h, n_e, m_e) = \Psi_e(n_e, z_e)\Psi_h(n_h, z_h)e^{-\lambda_1 r_{eh}}e^{-\lambda_2 r_{qe}}e^{i(m_e\theta_e + m_h\theta_h)}$,
where $\Psi_e(n_e, z_e)$ and $\Psi_h(n_h, z_h)$ are one-dimensional particle-in-a-box wavefunctions for the electron and hole along the nanotube's length:

$$\Psi_e(n_e, z_e) = \sqrt{\frac{2}{L}}\sin\left(\frac{n_e \pi z_e}{L}\right),$$

$$\Psi_h(n_h, z_h) = \sqrt{\frac{2}{L}}\sin\left(\frac{n_h \pi z_h}{L}\right).$$

The terms r_{eh}, r_{qe} and r_{qh} are the electron-hole, ion-electron, and ion-hole distances, respectively:

$$r_{eh} = \sqrt{4R^2\sin^2\left(\frac{\theta_h - \theta_e}{2}\right) + (z_h - z_e)^2}$$

$$r_{qe} = \sqrt{\left\{R^2 + \left(z_q - z_e\right)^2\right\}}$$

$$r_{qh} = \sqrt{R^2 + \left(z_q - z_h\right)^2}$$

The variational parameters λ_1 and λ_2 in the exponential terms represent the effective Coulomb interaction strengths between the exciton components and the ion.

The total Hamiltonian $\hat{H}$ is written as :
$\hat{H} = \hat{T} + \hat{V}$.

where the kinetic energy operator $\hat{T}$ includes both axial and angular motion of both the electron and the hole:

$$\widehat{T_z} = -\frac{\hbar^2}{2m_e^*}\frac{\partial^2}{\partial z_e^2} - \frac{\hbar^2}{2m_h^*}\frac{\partial^2}{\partial z_h^2}\ ,\ \widehat{T_\theta} = -\frac{\hbar^2}{2m_e^* R^2}\frac{\partial^2}{\partial \theta_e^2} - \frac{\hbar^2}{2m_h^* R^2}\frac{\partial^2}{\partial \theta_h^2}$$

The potential energy operator $\hat{V}$ accounts for the screened Coulomb interactions between the electron-hole pair and the ion:

$$\hat{V} = \widehat{V_{eh}} + \widehat{V_{qe}} + \widehat{V_{qh}},$$

with $\widehat{V_{eh}} = -\frac{e^2}{4\pi\varepsilon_{\text{eff}} r_{eh}}$, $\widehat{V_{qe}} = -\frac{e^2}{4\pi\varepsilon_{\text{eff}} r_{qe}}$, $\widehat{V_{qh}} = \frac{e^2}{4\pi\varepsilon_{\text{eff}} r_{qh}}$.

An effective dielectric constant $\varepsilon_{\text{eff}} = 9.0$ accounts for the dielectric screening within the nanotube environment.

The electron and hole effective masses are set to $m_e^* = m_h^* = 0.2m$, where m is the free electron mass. Additional simulations explore mass asymmetry by increasing either m_e^* or m_h^* by 25%.

The variational energy is obtained by minimizing

$$E(\lambda_1, \lambda_2) = \frac{\langle \psi_{\text{trial}} | \hat{H} | \psi_{\text{trial}} \rangle}{\langle \psi_{\text{trial}} | \psi_{\text{trial}} \rangle},$$

for each ion position z_q along the nanotube axis. Integrals are evaluated numerically using Gauss-Legendre quadrature (120 points for *z* and 40 points for *θ*), and the energy is minimized with respect to the variational parameters λ_1 and λ_2 using MATLAB's non-linear least squares minimizer.

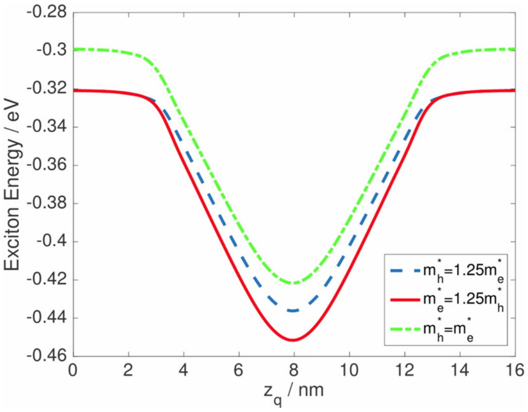

Supplementary Fig. 15. Proton-induced enhancement of electron–hole binding during exciton-proton encounters. Exciton binding energy was calculated as a function of proton position z_q along the axis of a defect-bearing (6,5)-SWCNT, based on the cylindrical shell model. As the proton approaches the defect-localized exciton, the electron–hole binding energy increases by up to ~0.13 eV, reflecting strong local electrostatic polarization during an exciton–proton encounter. Results are shown for three effective-mass scenarios: equal electron and hole masses (green dashed line), a heavier hole ($m_h^* = 1.25\, m_e^*$, blue dashed line), and a heavier electron ($m_e^* = 1.25\, m_h^*$, red solid line). The ion traverses the nanotube from $z_q = 0$ (left end) to $z_q = L$ (right end). The deepest energy minimum occurs when the proton is proximal to the defect site.

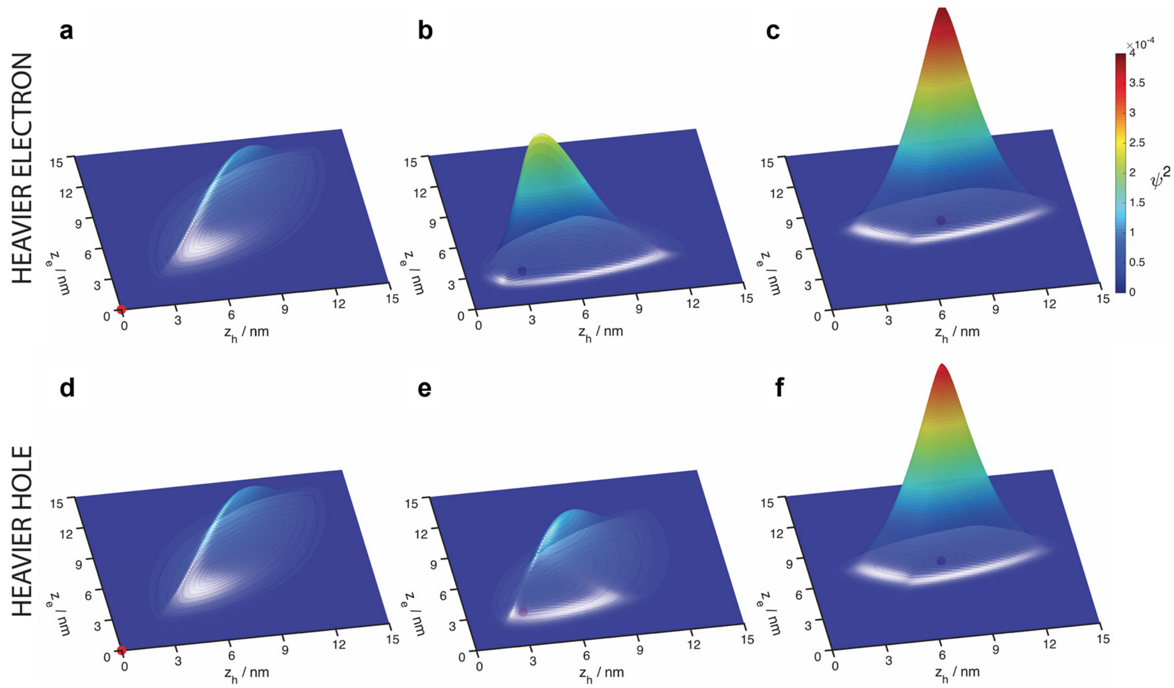

Supplementary Fig. 16. Local-field sensitivity of defect-trapped excitons. Calculated excitonic wavefunctions illustrate how an ion perturbs defect-trapped excitons inside a (6,5)-SWCNT pore. Shown are surface plots of the normalized squared excitonic wavefunction $|\psi|^2$ projected along the nanotube axis for three representative ion positions: $z_q = 0$ nm (near the pore entrance), $z_q = 3$ nm, and $z_q = 7.5$ nm (near the center of the pore). Results are shown for cases with (**a**–**c**) heavier electrons (+25%) and (**d**–**f**) heavier holes (+25%), exhibiting robustness of the response to effective-mass asymmetry. The ion position is indicated by a red dot in each panel. As the ion approaches the defect site, the excitonic wavefunction becomes increasingly compressed and polarized, reflecting strong local electrostatic coupling during an exciton–ion encounter.

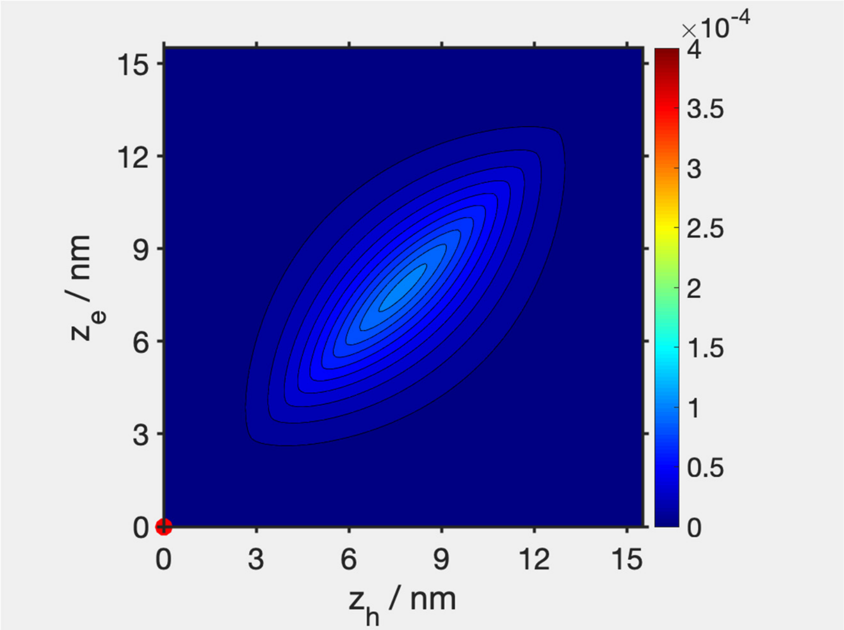

Supplementary Video 1 | Computational model of an exciton–ion collision inside a carbon nanotube pore. Visualization of the calculated excitonic wavefunction in a (6,5)-SWCNT as a positively charged ion (red dot) approaches and traverses the nanotube. The color map shows the normalized squared excitonic wavefunction amplitude (|ψ|²), illustrating how the spatial distribution of the electron–hole pair is distorted by the ion's local electrostatic field. The simulation is based on the cylindrical-shell model described in Supplementary Fig. 14 and captures the microscopic mechanism underlying the experimentally observed exciton–ion collisions. As the ion approaches the exciton localization region, the enhanced electron–hole binding and wavefunction distortion provide a physical basis for the discrete, reversible spectral shifts observed for exciton–proton collisions in confined water.

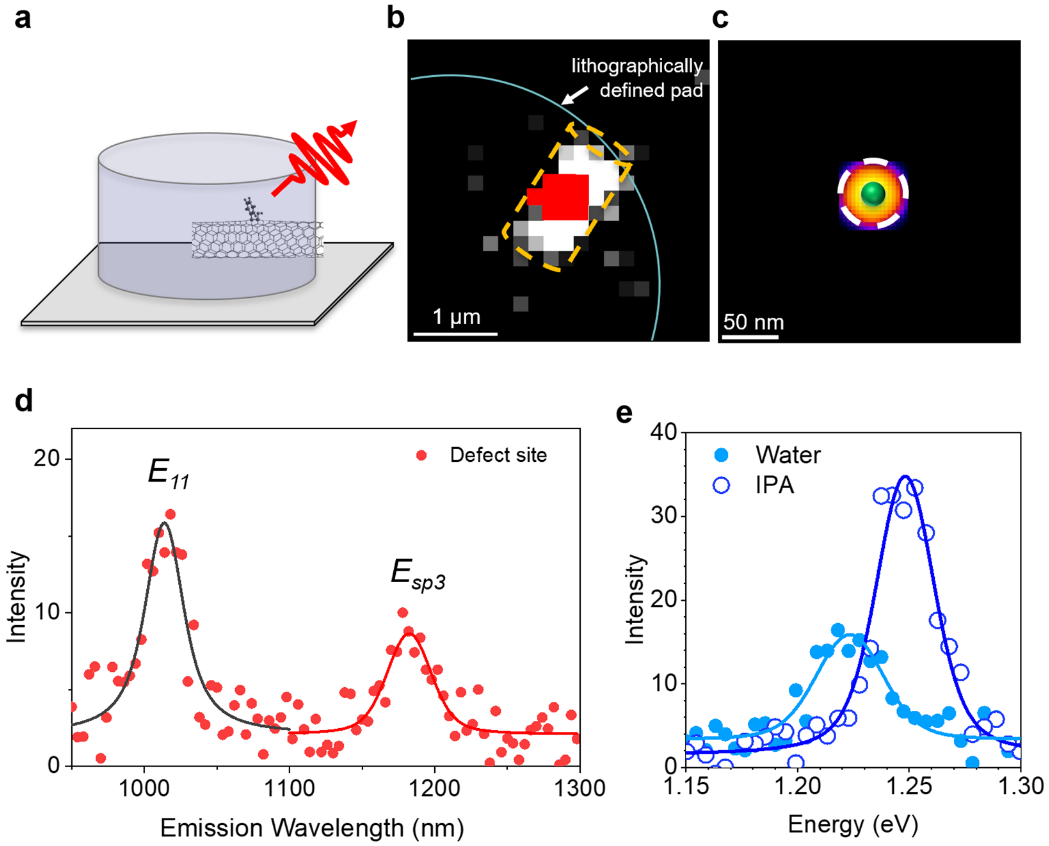

Supplementary Fig. 17. Extended dataset of Fig. 4 demonstrating repeated exciton–proton encounters at a *single, spatially localized defect trap* within a short, open-ended (6,5)-SWCNT. **a,** Schematic illustration of a short SWCNT containing a single sp^3 quantum defect site and embedded in a TIP device to allow controlled access of aqueous solutions through the exposed nanotube end. **b,** Superimposed PL image showing nanotube emission (E_{11}, white) and defect-trapped exciton emission (E_{sp3}, red) within a lithographically defined Parylene C pad. **c,** Super-resolution localization map of the defect-trapped exciton, confirming that all measurements originate from the same atomic defect site (localization precision <20 nm). **d,** PL spectrum recorded from the localized defect site, showing both mobile (E_{11}) and defect-trapped (E_{sp3}) exciton emission, confirming the presence of a single exciton trap within the nanotube pore. **e,** PL spectra from the same defect site measured in dry IPA and water, showing a reversible spectral shift of E_{11} that confirms nanopore accessibility to molecular filling.

Time-resolved PL measurements from this same defect site under mildly acidic conditions (pH 5.9) exhibit discrete, reversible intensity steps arising from repeated proton trapping and de-trapping events. Because all spectral and temporal data are collected from the same spatially localized defect, these measurements demonstrate the ability to repeatedly probe exciton–proton collisions at a single atomic site over time, rather than averaging over different defects or nanotubes.

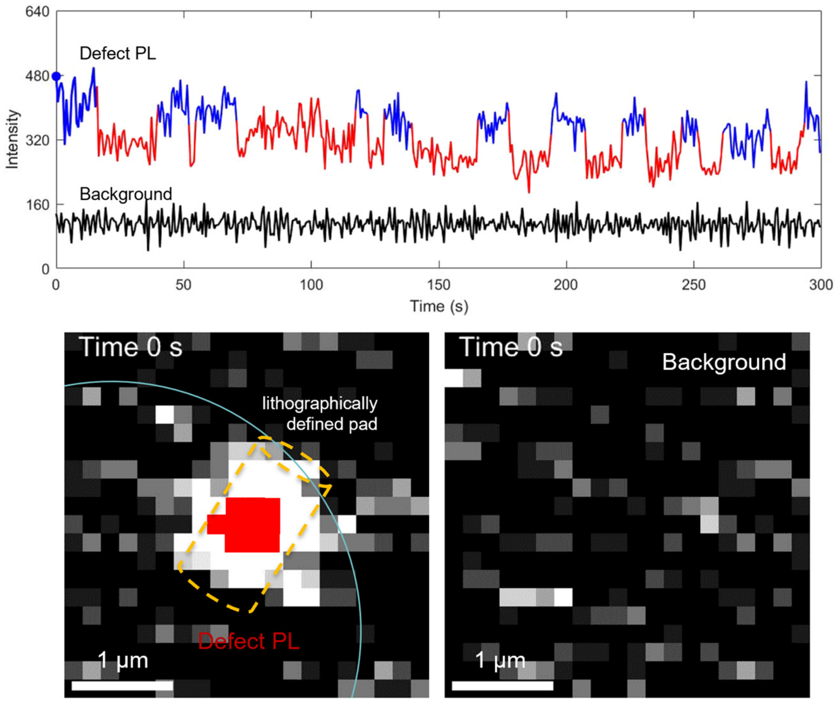

Supplementary Video 2 | Spectral response to exciton–proton collisions at a single defect trap in a short nanotube pore. Time-resolved photoluminescence (PL) responses to exciton–proton collisions at a single defect trap in a TIP device containing a *short, open-ended* (6,5)-SWCNT exposed to a pH 2.0 aqueous solution. The data were recorded from the same individual nanotube and the same atomic defect site shown in Supplementary Fig. 17 and Fig. 4 of the main text. Discrete, reversible intensity steps (highlighted in red) arise from individual proton trapping and de-trapping events at the defect-localized exciton, while the black trace represents a background reference signal acquired from a nearby, defect-free region. This video directly visualizes repeated exciton–proton collisions at a single defect trap under strongly acidic conditions, demonstrating the ability to monitor ion–exciton interactions within an individual carbon nanotube nanopore.

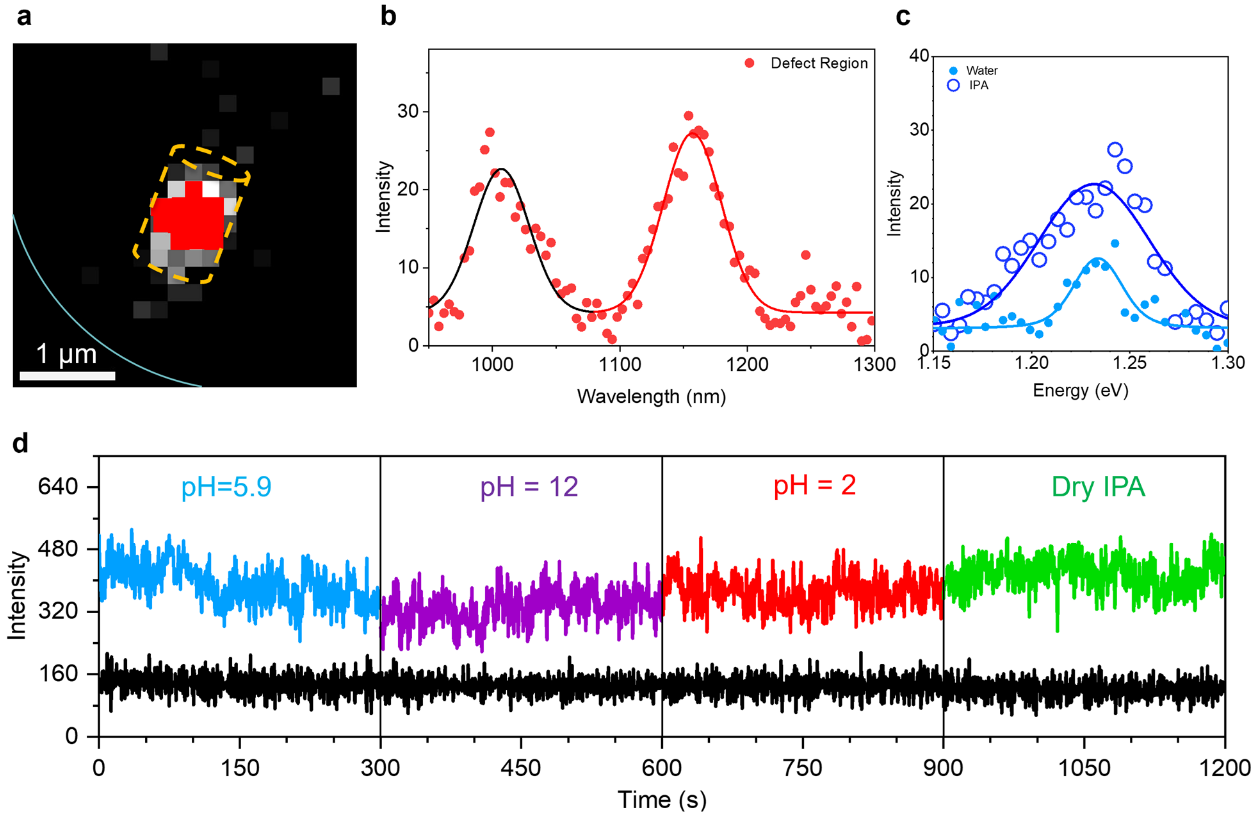

Supplementary Fig. 18. Negative control: no pore access, no exciton–proton collision signatures. Control experiment demonstrating the absence of exciton–proton interaction signatures in a *fully encapsulated* SWCNT, where the nanotube pore is inaccessible to water and ions. **a,** PL image of a defect-bearing (6,5)-SWCNT that is fully encapsulated, showing overlaid mobile nanotube exciton emission (E_{11}, white) and defect-trapped exciton emission (E_{sp3}, red). **b,** PL spectrum recorded from the defect region, showing well-resolved E_{11} and E_{sp3} emission peaks. **c,** PL spectra measured from the same defect site under immersion in water and dry IPA, showing no detectable E_{11} energy shifts, consistent with the absence of molecular access to the nanotube interior. **d,** Time-resolved PL intensity traces of the same defect trap under sequential exposure to mildly acidic water (pH 5.9), strongly basic solution (pH 12), strongly acidic water (pH 2), and dry IPA. No discrete intensity steps, spectral shifts, or stochastic switching events are observed under any condition.

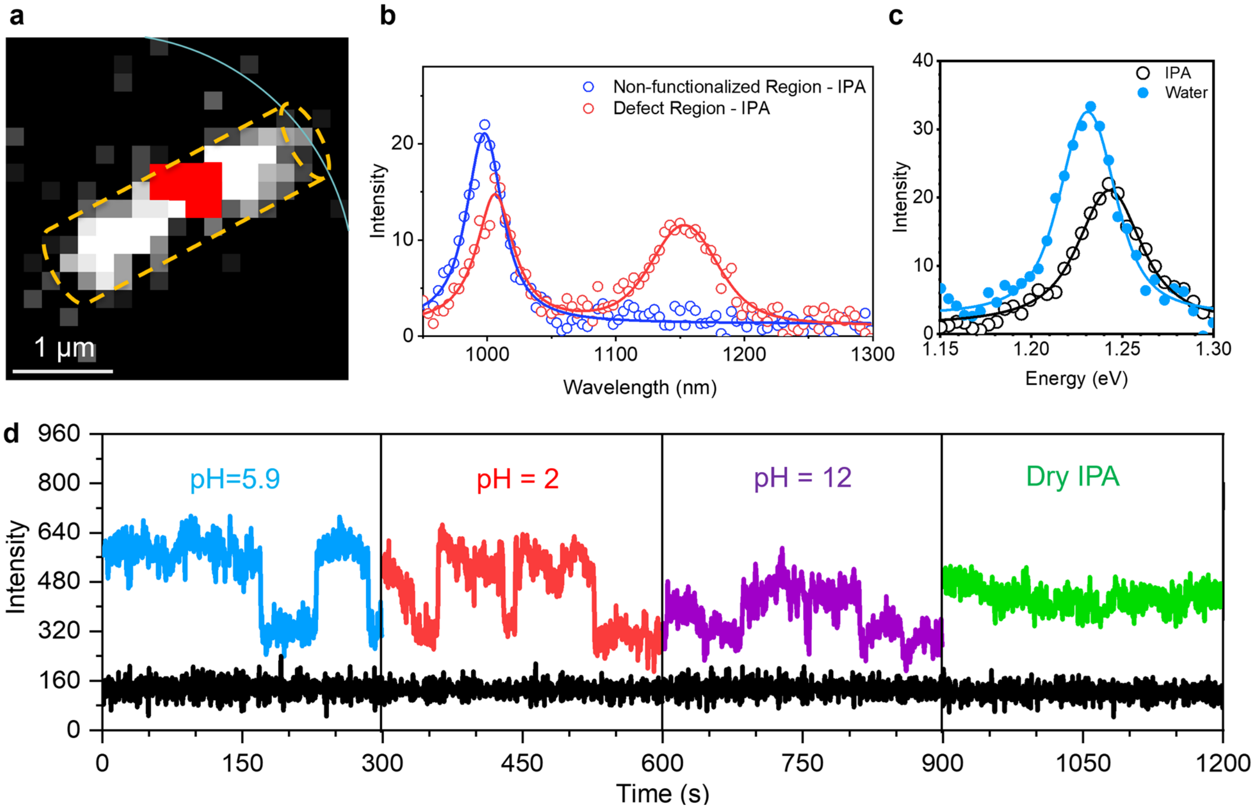

Supplementary Fig. 19. Reduced exciton–proton collision probability for defect sites deeper within nanotube pores. Spatial dependence of exciton–proton collision signatures in a TIP device containing a *single long* (6,5)-SWCNT with one open end. **a,** Superimposed PL image showing mobile nanotube exciton emission (E_{11}, white) and defect-trapped exciton emission (E_{sp3}, red) from a long, open-ended (6,5)-SWCNT. The dashed outline indicates the nanotube axis and defect location relative to the exposed pore mouth. **b,** PL spectra collected from an unfunctionalized nanotube region and from the defect site under dry IPA conditions, confirming the presence of a single defect-localized exciton trap. **c,** Comparison of PL spectra acquired under water and dry IPA exposure, showing E_{11} energy shifts that confirm nanopore accessibility in the long nanotube geometry. **d,** Time-resolved PL intensity traces of defect-trapped excitons (E_{sp3}) recorded from individual defect sites located at different axial positions within long SWCNT pores under sequential exposure to mildly acidic water (pH 5.9), strongly acidic water (pH 2), strongly basic solution (pH 12), and dry IPA. Defect sites located farther from the pore mouth exhibit a ~75% reduction in the frequency of discrete intensity steps compared to near-mouth defects.

This pronounced spatial dependence demonstrates that exciton–proton collision probability decreases with increasing distance from the pore entrance, consistent with reduced proton accessibility in deeper regions of the nanotube. These results further confirm that the discrete PL intensity steps observed throughout this work arise from pore-confined proton encounters with defect-localized excitons, rather than from surface adsorption or global environmental fluctuations. Data shown are representative of measurements performed across multiple independent nanotube–defect devices.

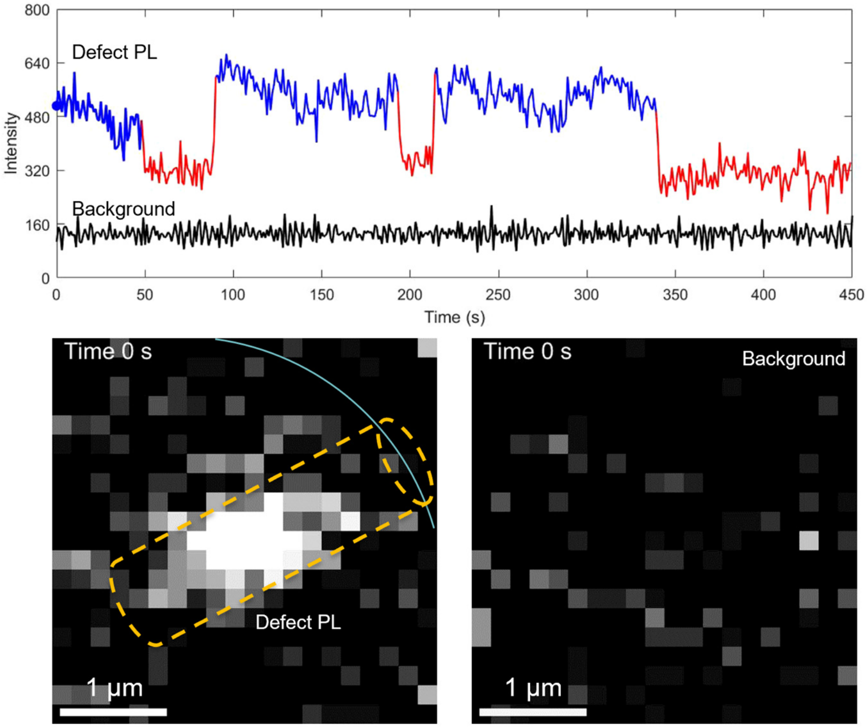

Supplementary Video 3 | Exciton–proton collisions at a single defect site under strongly acidic conditions. Photoluminescence monitoring of exciton–proton collisions at a defect trap in a TIP device containing a long, open-ended (6,5)-SWCNT as the nanotube pore fills with a pH 2.0 aqueous solution. The data correspond to the *same individual nanotube and the same atomic defect site* shown in Supplementary Fig. 19. Discrete, reversible intensity steps (highlighted in red in the intensity trace) arise from repeated proton trapping and de-trapping events at the defect-localized exciton, while the black trace represents a background reference signal. The accompanying PL images show the spatially localized defect emission within the nanotube during the measurement. This video directly visualizes exciton–proton collision dynamics at a single defect trap and illustrates how increasing proton availability leads to more frequent encounters, consistent with the stepwise intensity trajectories analyzed in the main text and Supplementary Figs. 17–20.

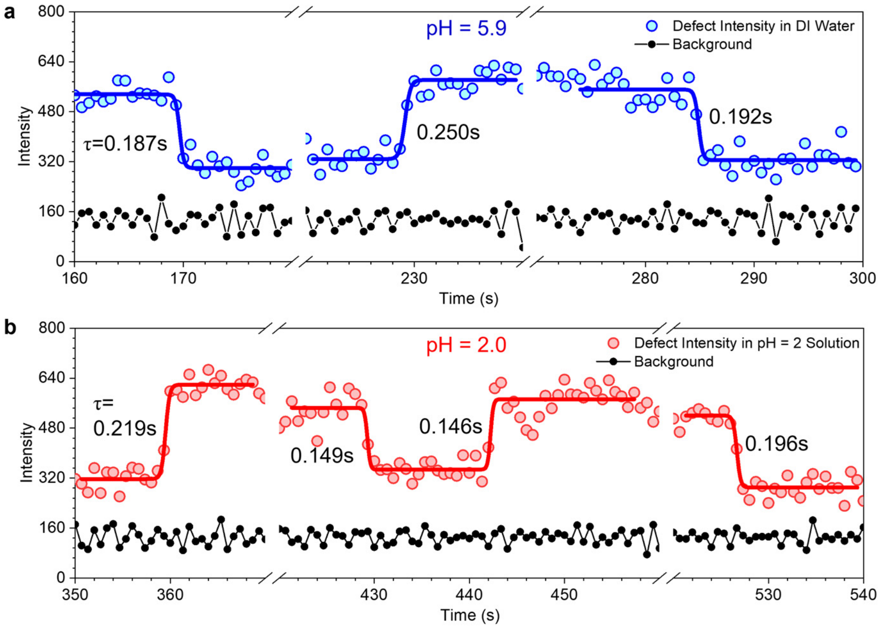

Supplementary Fig. 20. Kinetics of single-proton trapping and de-trapping at an individual defect trap. Time trace of photoluminescence responses to exciton-proton interactions at a *single defect-trap* showing discrete transitions associated with proton occupancy at the same atomic defect site. **a,** Logistic fitting of individual PL intensity steps recorded from the defect-trapped exciton in water (pH 5.9). **b,** Logistic fitting of PL intensity steps recorded from the *same defect site* in an acidic solution (pH 2.0). Each discrete intensity transition corresponds to a single proton trapping or de-trapping event at the defect trap and is well described by a sigmoidal (logistic) function. The extracted time constants (τ) quantify the characteristic kinetics of stochastic proton occupancy at an individual exciton trap, rather than ensemble-averaged behavior. While trapping time constants are comparable across pH conditions, de-trapping transitions occur more rapidly at lower pH, consistent with increased proton–proton electrostatic repulsion at higher proton concentrations. All traces are recorded from the *same defect trap* shown in Supplementary Fig. 17, demonstrating repeatable, site-specific proton interaction kinetics at a single atomic defect within a nanotube pore.

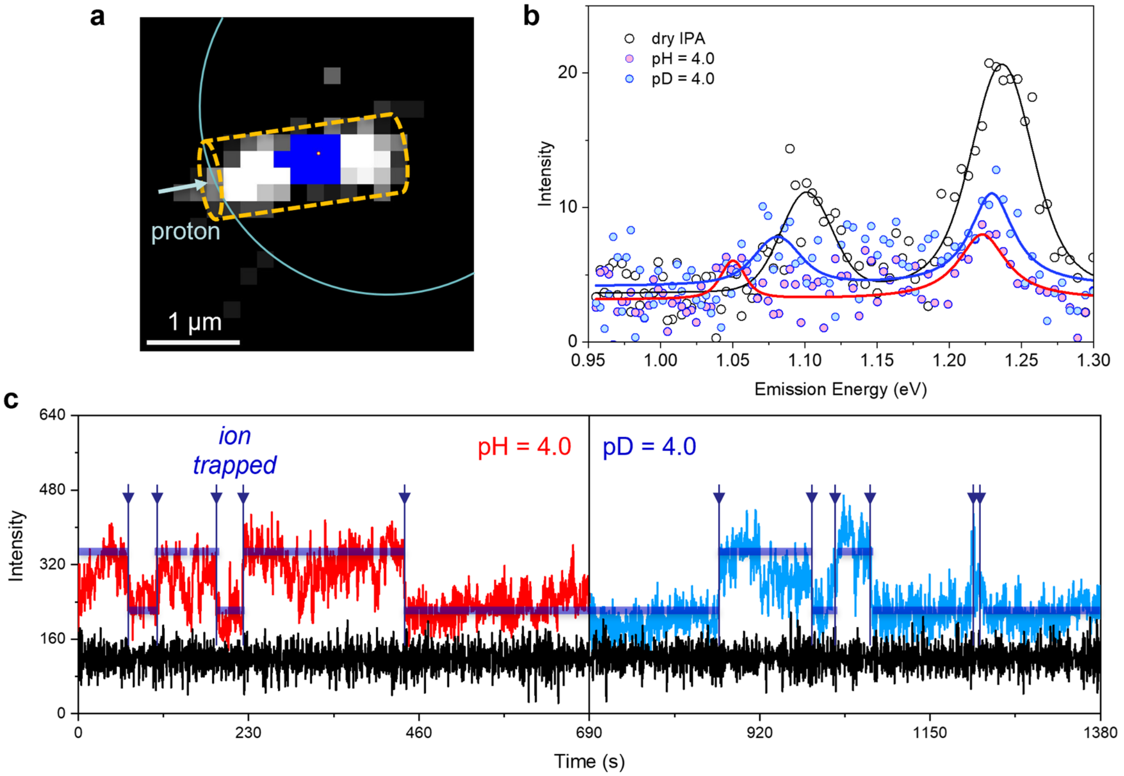

Supplementary Fig. 21. Kinetic isotope effect confirms hydrated proton identity in exciton–proton collisions. Isotope-dependent kinetics of ion trapping at a *single defect trap* demonstrate that the mobile species responsible for the observed collision signatures is the hydrated proton. **a,** PL image of a 3,4,5-trifluorobenzene defect-functionalized (6,5)-SWCNT showing E_{11} (white) and defect (E_{sp3}, blue) emissions. The dot indicates the super-resolved defect site. The highlighted pixel marks the super-resolved defect site monitored throughout the experiment. **b,** PL spectra of the same defect site measured in dry IPA, H_2O (pH 4.0), and D_2O (pD 4.0), showing distinct spectral responses associated with molecular and isotopic filling of the nanotube pore. **c,** Time-resolved PL intensity trajectories of the defect-trapped exciton recorded sequentially in H_2O (pH 4.0, red) and D_2O (pD 4.0, blue). Discrete intensity plateaus correspond to ion trapping events at the same atomic defect site. Deuterons exhibit systematically longer dwell times than protons, with an average dwell-time ratio of 1.54 ± 0.22 for the single defect shown and 1.40 ± 0.20 averaged across five independent defect sites. The observed kinetic isotope effect, manifested as prolonged occupancy in D_2O relative to H_2O, provides independent evidence that the observed exciton–ion collision signatures arise from hydrated protons (and deuterons), rather than from nonspecific ionic or molecular interactions.